Supporting Information

Electronic transmission bridge via 3D N-doping steering urea electrosynthesis

Yue Lv, Xiong Zhang, Han-wen Wang, Yi-hong Zhu, Zhuang Hu, Yang-wen Wu*, Qiang Lu*

National Engineering Research Center of New Energy Power Generation,
North China Electric Power University, Beijing 102206, China

Supporting Information Content:

Text S1 calculation details:

Spin-polarized first-principles calculations were performed using the Vienna Ab initio Simulation Package (VASP), based on density functional theory (DFT) [1]. The Perdew-Burke-Ernzerhof (PBE) functional within the generalized gradient approximation (GGA) was employed for exchange-correlation, with ultrasoft pseudopotentials for core electrons. Weak van der Waals interactions were accounted for using Grimme's D3 correction [2, 3]. Through truncation energy testing, the plane-wave basis set energy cutoff was set to 400 eV (Fig. S28), and self-consistent field (SCF) convergence was achieved when the energy change per atom was below 10^{-6} eV. Catalyst models were constructed as 4N-saturated nitrogen-doped Cu single-atom catalysts (Cu-N_4-C SAC), and 5N 3D nitrogen-doped Cu single-atom catalysts (Cu-N_5-C SAC) on graphene, using a 5×6×1 graphene supercell with a 15 Å vacuum layer along the z-axis to eliminate periodic image interactions [4]. Gas molecules were calculated in 12×14×15 Å cell lattices. Structures were optimized until Hellmann-Feynman forces were below 0.01 eV/Å. The irreducible Brillouin zone was sampled with a 2×2×1 k-point grid centered at Γ for structure optimization, and a 3×3×1 k-point grid for static calculations [5]. A denser 9×9×1 k-point mesh was used for density of states (DOS) calculations. Electronic structure analyses, including DOS, projected density of states (PDOS), crystal orbital Hamiltonian population (COHP), and charge density difference (CDD), were conducted to characterize orbital interactions, bond strengths, and electron transfer between metals and adsorbates [6-8].

The initial configuration was geometrically optimized to obtain the stable

adsorption configuration with the lowest energy, and the surface configuration of the Cu-N-C SAC catalyst was investigated by examining the distances between specific atoms in the configuration and their adsorption energies. The adsorption energy Eads of the molecules on the catalyst surface can be calculated from equation (1):

$$E_{ads} = E_{sys} - E_{catal} - E_{gas} \quad (1)$$

Where E_{sys}, E_{catal}, and E_{gas} denote the energy of the whole adsorption system, the energy of the catalyst surface, and the gas phase molecules before adsorption in eV, respectively.

The charge density difference ($\Delta\rho$) describes the charge transfer that occurs on the surface of the catalyst after adsorption of the reactants and can be calculated from equation (2):

$$\Delta\rho = \rho_{sys} - \rho_{catal} - \rho_{ads} \quad (2)$$

where ρ_{sys} denotes the electron density of the adsorbed configuration, ρ_{catal} denotes the electron density of the catalyst on which no adsorption occurs, and ρ_{ads} denotes the electron density of the adsorbate.

The thermodynamic calculations are based on the Computational Hydrogen Electrode (CHE) model, taking into account the effects of potential (U) and pH (assuming pH=0), and are calculated as follows.

$$\Delta G = \Delta E + \Delta E_{ZPE} - T\Delta S + \Delta G_U + \Delta G_{pH} \quad (3)$$

where ΔE is the electronic energy difference between the free and adsorbed states of the reacting intermediate, which can be obtained directly by DFT calculations. Typically, the most stable structures of successive intermediates inevitably deform

throughout the chemical reaction. In this work, a static surface is used for each electrical step to calculate the reaction energy, excluding the generation energy of the intermediates. ΔE_{ZPE} is the change in vibrational energy for zero pints, and $T\Delta S$ is the entropy contribution at room temperature. For each reactant, its ΔE_{ZPE} and $T\Delta S$ can be calculated by the following equations.

$$E_{ZPE} = \frac{\sum_i h\nu_i}{2} \tag{4}$$

$$TS = RT\sum_i [\frac{h\nu_i}{k_B T} \frac{1}{e^{\frac{h\nu_i}{k_B T}} - 1} - \ln(1 - e^{-\frac{h\nu_i}{k_B T}})] \tag{5}$$

where k_B denotes Boltzmann's constant, h is Planck's constant, ν_i denotes the frequency of the adsorbed substance, R is the ideal gas constant. T is the temperature of the system, which was set here to 298.15 K. ΔG_U is the free energy contribution associated with the applied potential U. U is the operating electrochemical potential relative to the repotential Reversible Hydrogen Electrode (RHE). ΔG_{pH} is the calibrated concentration of H^+, $\Delta G_{pH} = k_B T \times \ln 10 \times pH$ .In this work, the pH is assumed to be 0 in highly acidic solutions. In addition, the kinetics were used to determine the transition states and calculate the reaction energy barriers using the climbing image nudged elastic band (CI-NEB) method. The configurations involved in the CO_2 reduction reaction (CO_2RR) and NO reduction reaction (NORR) reaction processes include the intermediate (IM), transition state(intermediate, IM), transition state (TS) and final state (FS), where each transition state (TS) was obtained by searching with the Cl-NEB method, and the energy barriers ($E_{barrier}$) of the chemical reactions were calculated by Eq. (6):

$$E_{barrier} = E_{transitio\ state} - E_{intermediate} \quad (6)$$

where $E_{transitio}$ state and $E_{intermediate}$ refer to the TS and IM energies, respectively.

We carried out ab initio molecular dynamics (AlMD) simulation at 298 K and constructed the free energy profiles. A 1 fs time step with hydrogen mass set to 2 and the convergence criteria for the electronic step set to $1x10^{-6}$ eV using the gamma point of the Brillouin zone [9].

We applied an external macroscopic electric field within VASP, imposing a uniform electrostatic field across the entire periodic system. This principle alters the electron cloud distribution and band structure through Coulomb interactions between the electric field and electrons, whilst introducing dipole corrections to eliminate dipole interference between adjacent unit cells under periodic boundary conditions. Enable LDIPOL = .TRUE. to perform dipole moment correction, thereby eliminating computational artifacts induced by surface asymmetry. Set IDIPOL = 3 to designate the z-axis as the correction direction, consistent with the practical electric field configuration. An external electric field of 0.1 eV/Å is imposed via the EFIELD parameter. This parameter combination enables precise calculation of key properties of the system under electric field modulation, offering robust support for elucidating the underlying regulation mechanism.

Supplementary Fig:

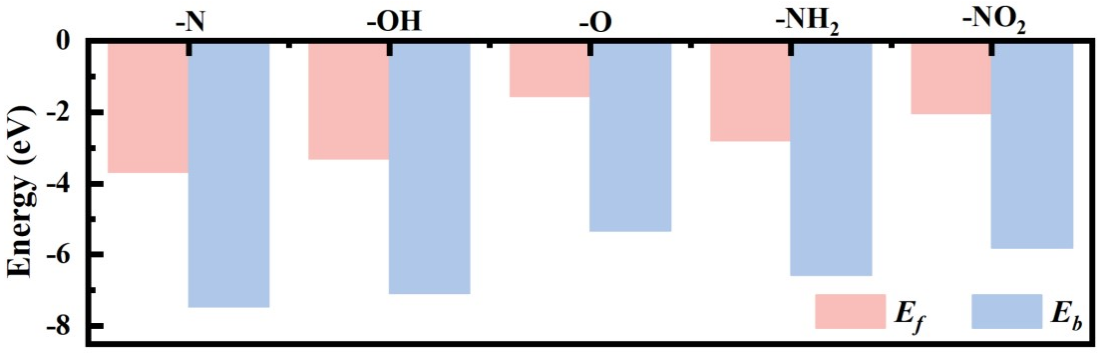

Fig. S1 Comparison of formation energies and binding energies for multiple axial coordination surfaces.

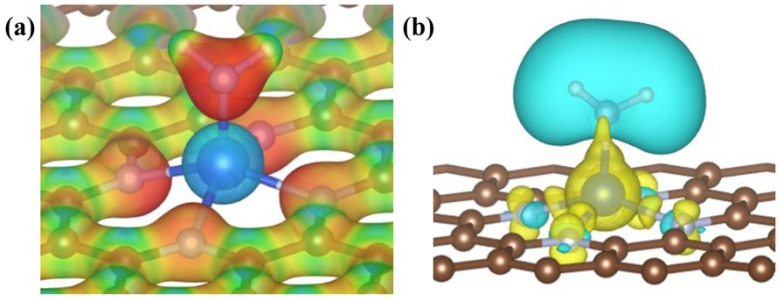

Fig. S2. Electronic structure of the NH_2 axial ligand catalyst. (a) Electrostatic potential. (b) Charge density distribution.

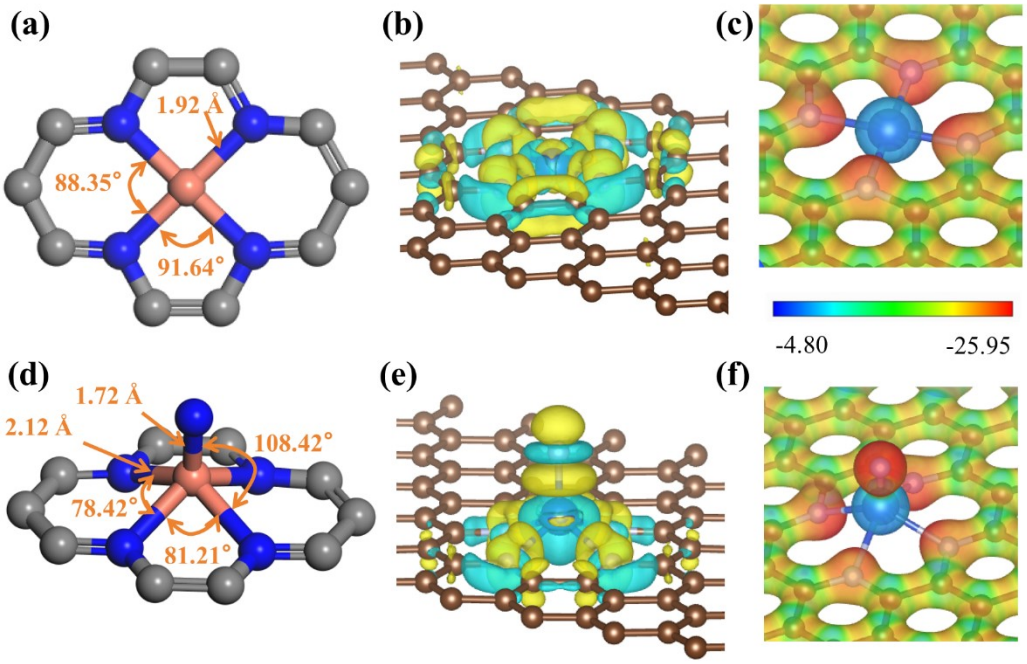

Fig. S3. Effect of pyridinic 3D N form of Cu-N-C SAC.

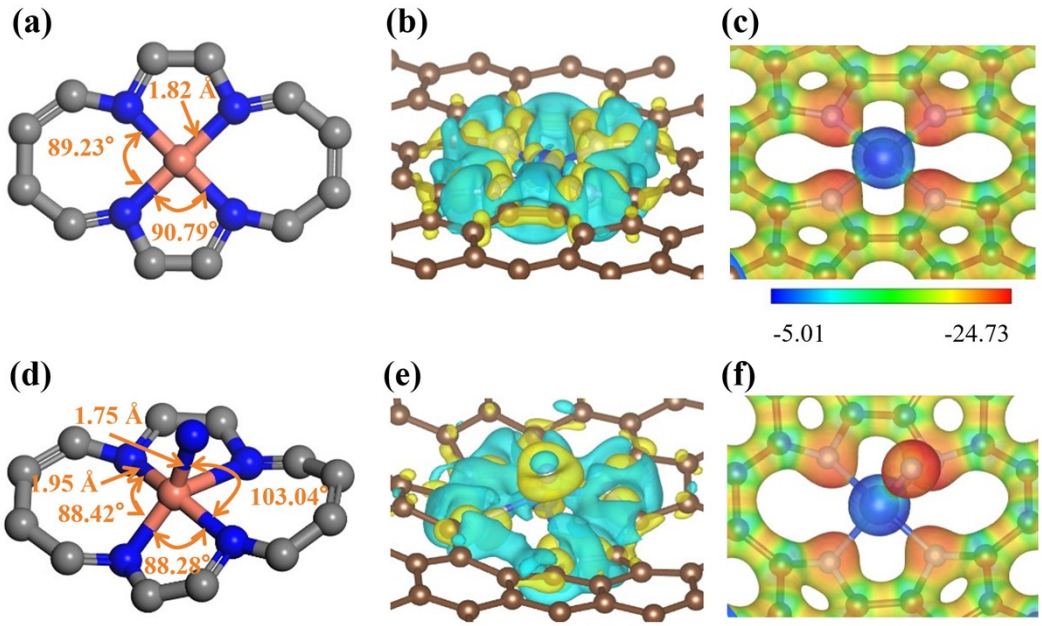

Fig. S4. Effect of pyrrolic 3D N form of Cu-N-C SAC.

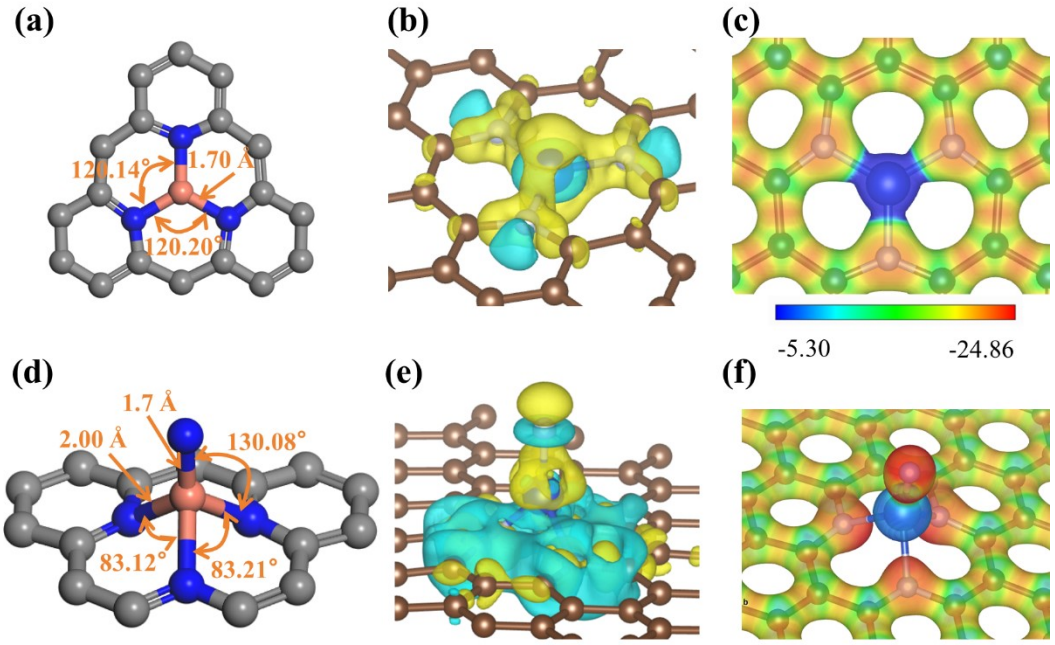

Fig. S5. Effect of graphitic 3D N form of Cu-N-C SAC.

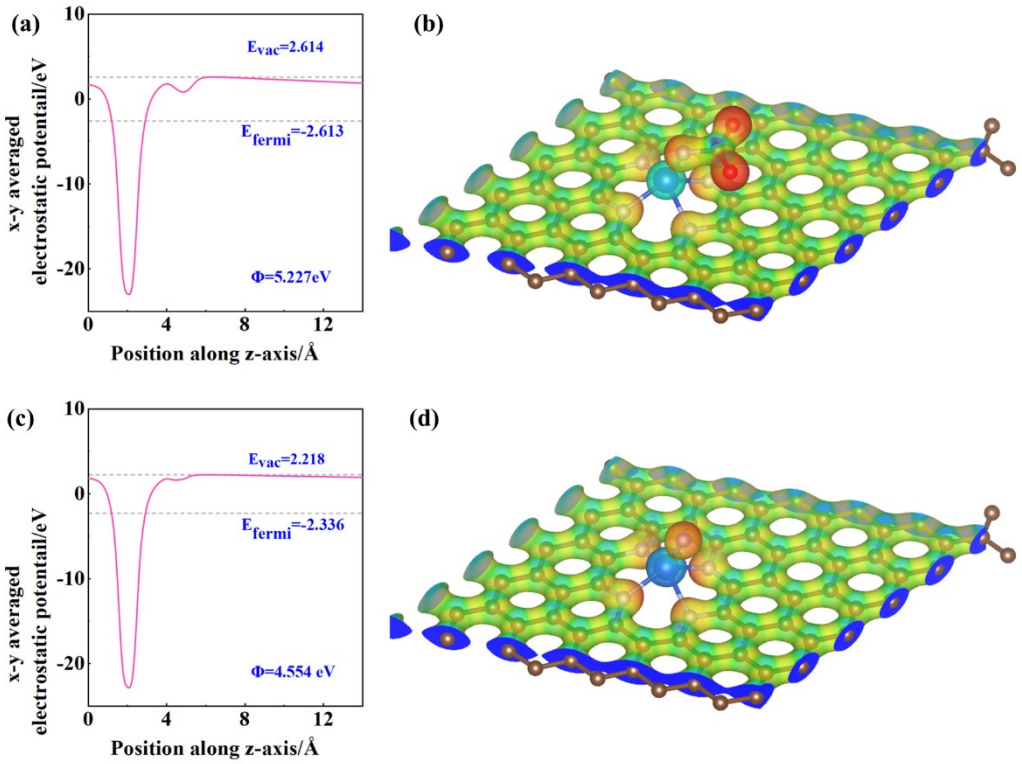

Fig. S6. Cu-N_5-C SAC adsorption of *CO_2. (a) Work function diagram of Cu-N_5-C SAC adsorbed *CO_2. (b) Electrostatic potential diagram of Cu-N_5-C SAC adsorbed *CO_2. (c) Work function diagram of Cu-N_5-C SAC. (b) Electrostatic potential diagram of Cu-N_5-C SAC.

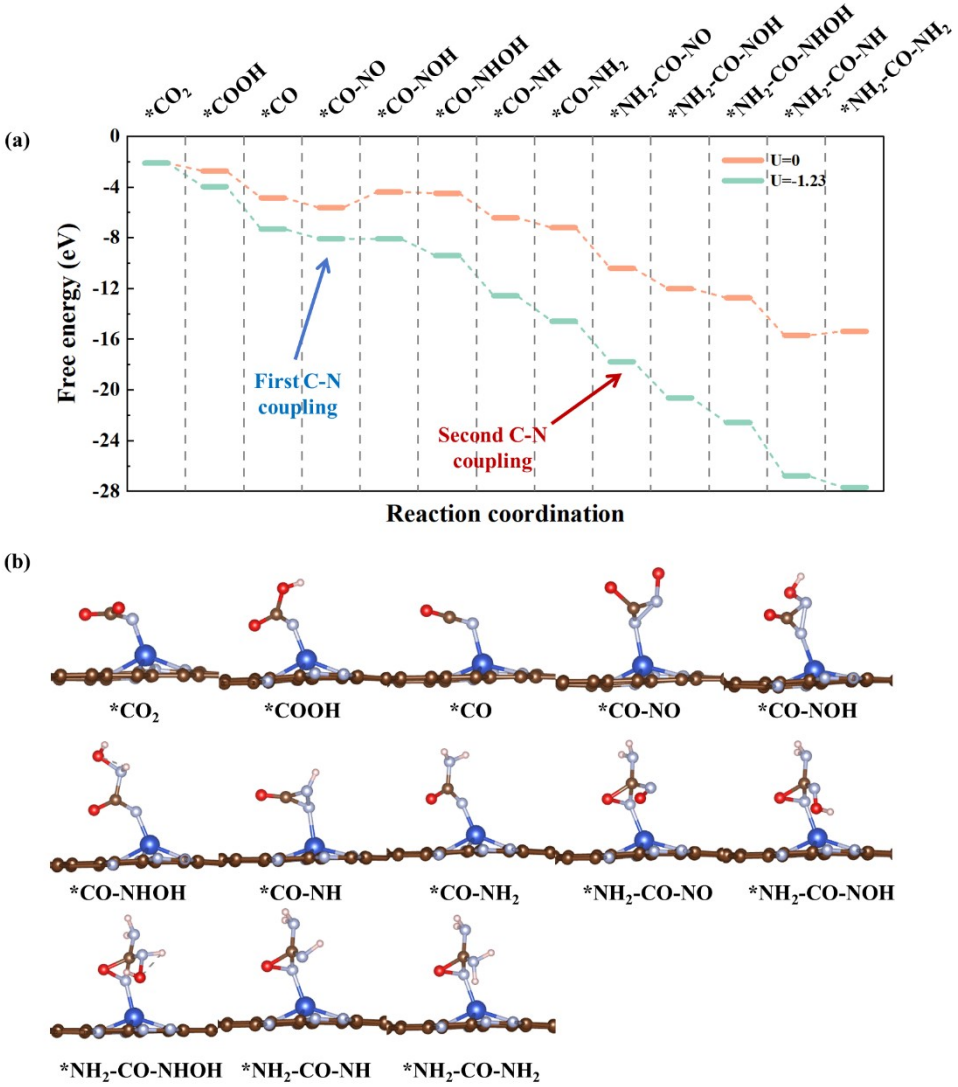

Fig. S7. (a) Free energy curves for electrochemical urea production on Cu-N_5-C SAC. (b) Side view of all optimized possible reaction intermediates for urea production on Cu-N_5-C SAC.

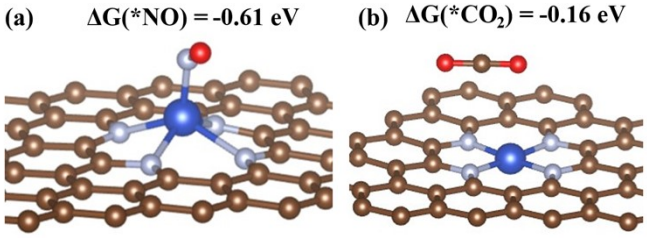

Fig. S8. The adsorption energies of CO_2 and NO on the Cu-N_4-C SAC. (a) NO. (b) CO_2.

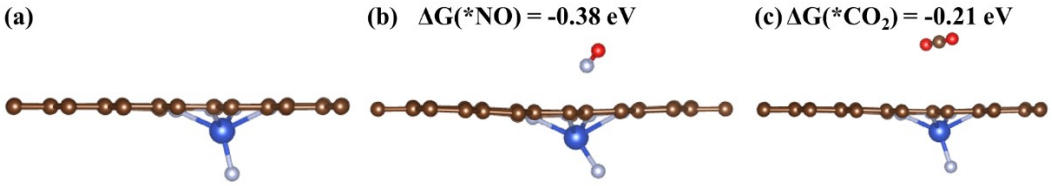

Fig. S9. Calculation of NO and CO_2 adsorption on N-Cu-N_4-C SAC with the active center of Cu.

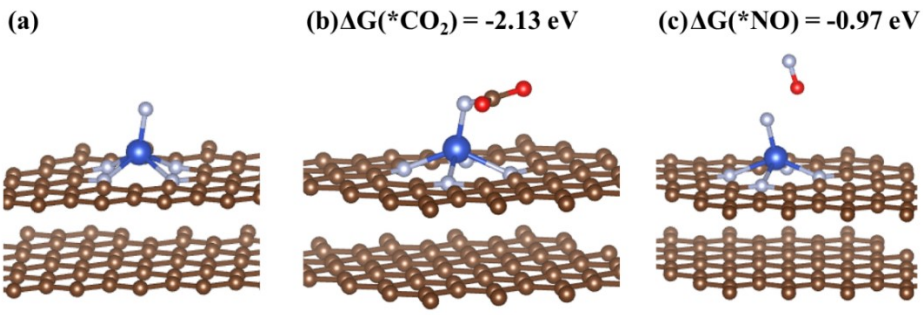

Fig. S10. (a) Double layer graphene surface. (b) Adsorption structure and energy of CO_2. (c) Adsorption structure and energy of NO.

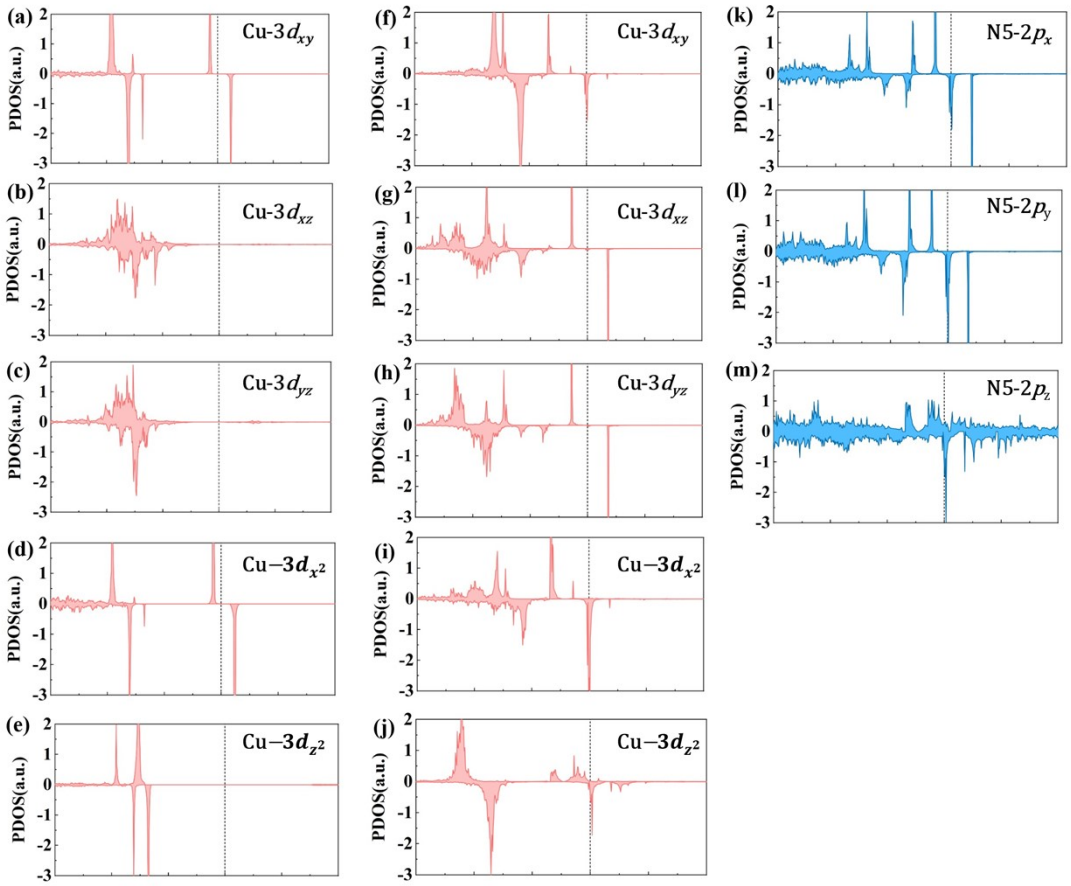

Fig. S11. Comparison of DOS on 3D N-modified surfaces. (a-e) Cu-N_4-C SAC. (f-m) Cu-N_5-C SAC.

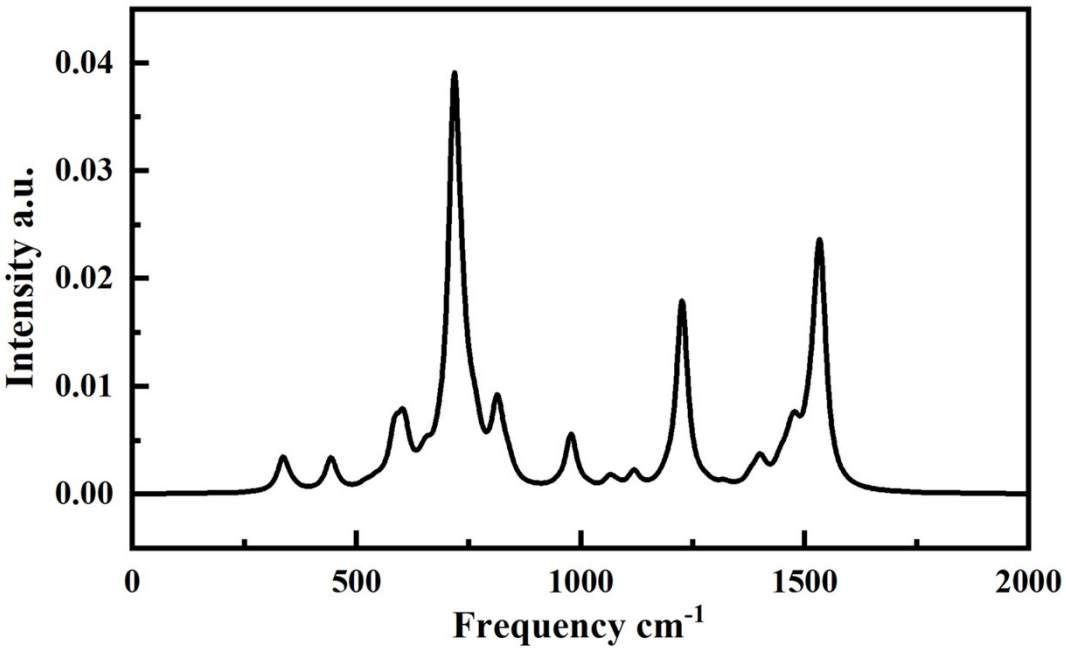

Fig. S12. Raman spectra of Cu-N_5-C SAC.

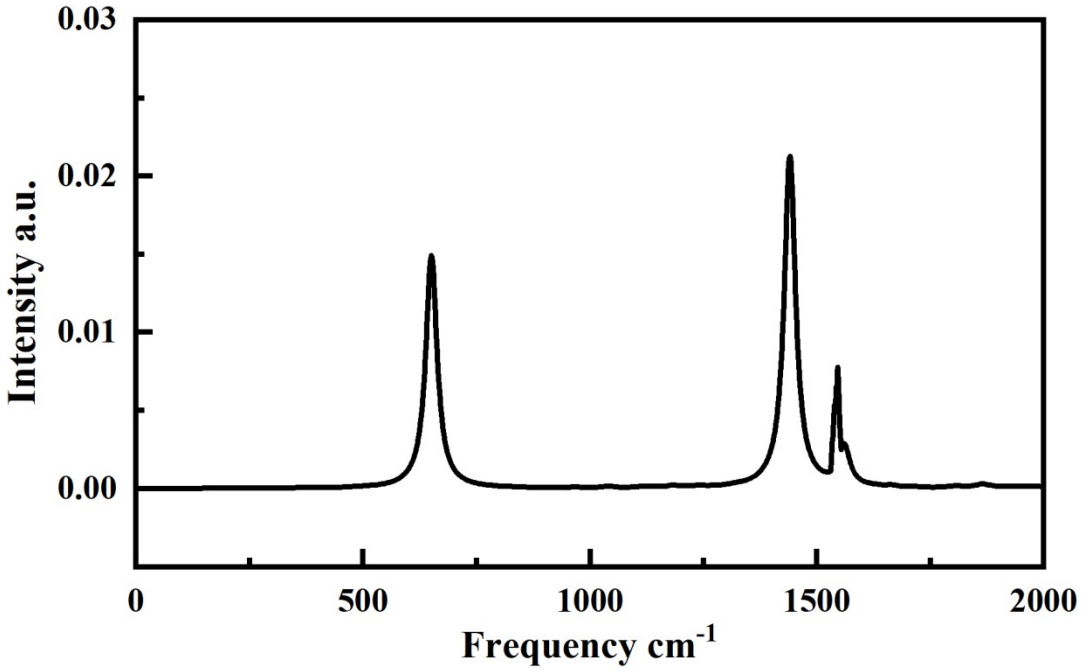

Fig. S13. Raman spectra of Cu-N_4-C SAC.

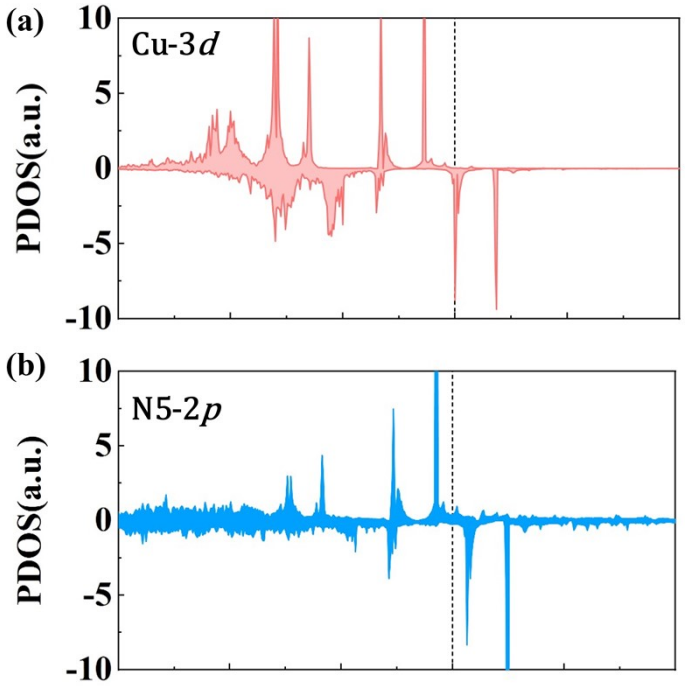

Fig. S14. PDOS of Cu-N_5-C SAC. (a) Cu d orbital. (b) N p orbital.

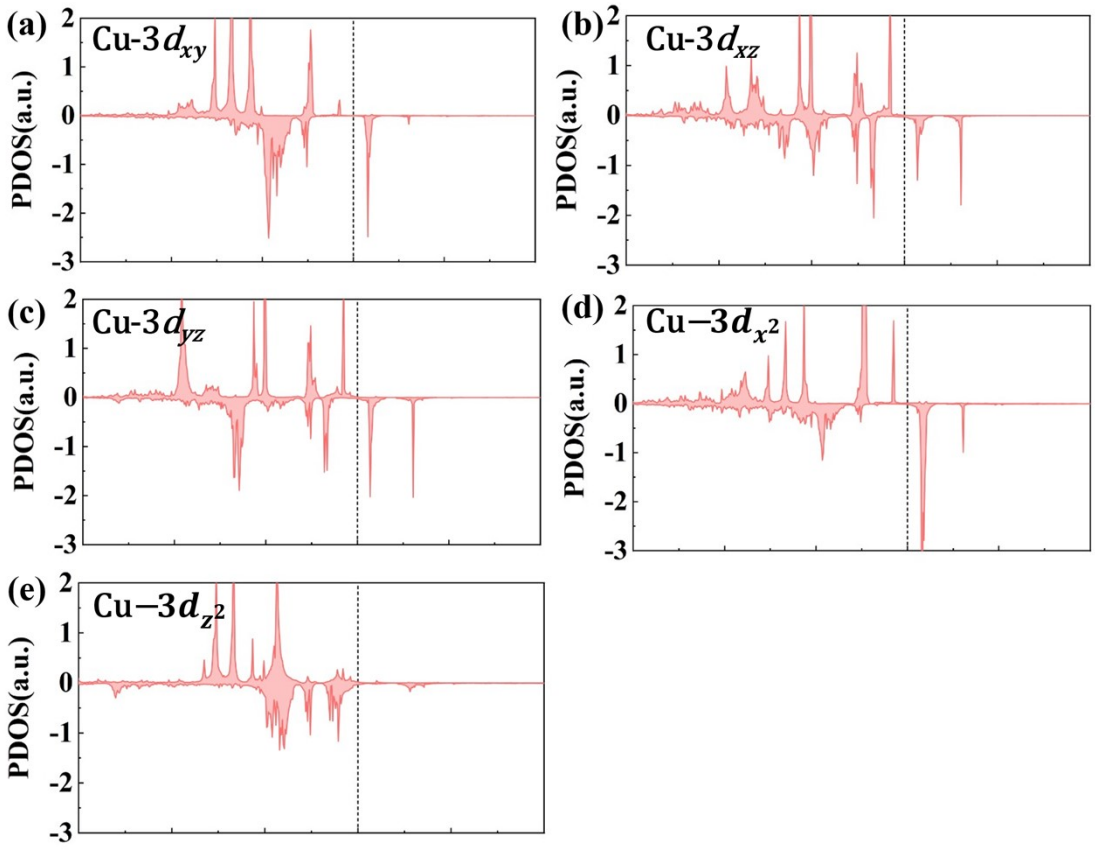

Fig. S15. PDOS of Cu d orbitals after CO_2 adsorption by Cu-N_5-C SAC.

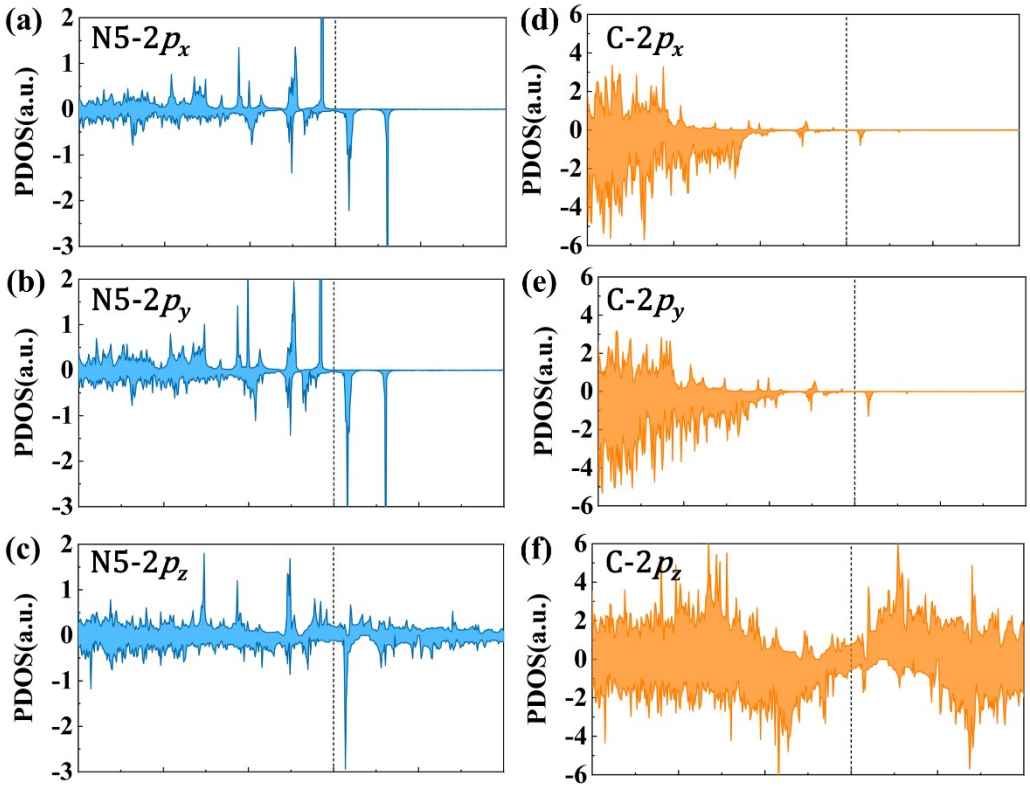

Fig. S16. PDOS of N_5 p and C p orbitals in Cu-N_5-C SAC after adsorption of CO_2.

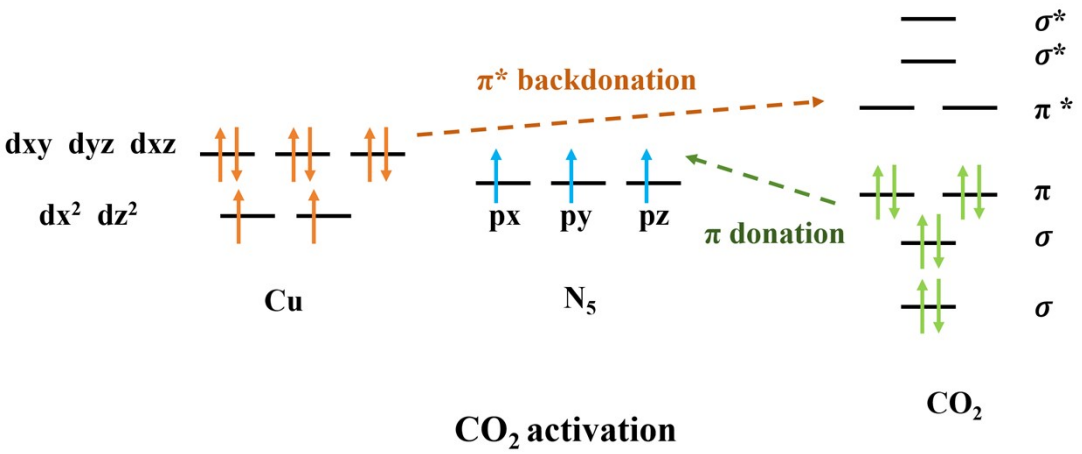

Fig. S17. Schematic representation of the role of 3D N_5 in the CO_2 activation of Cu-N_5-C SAC.

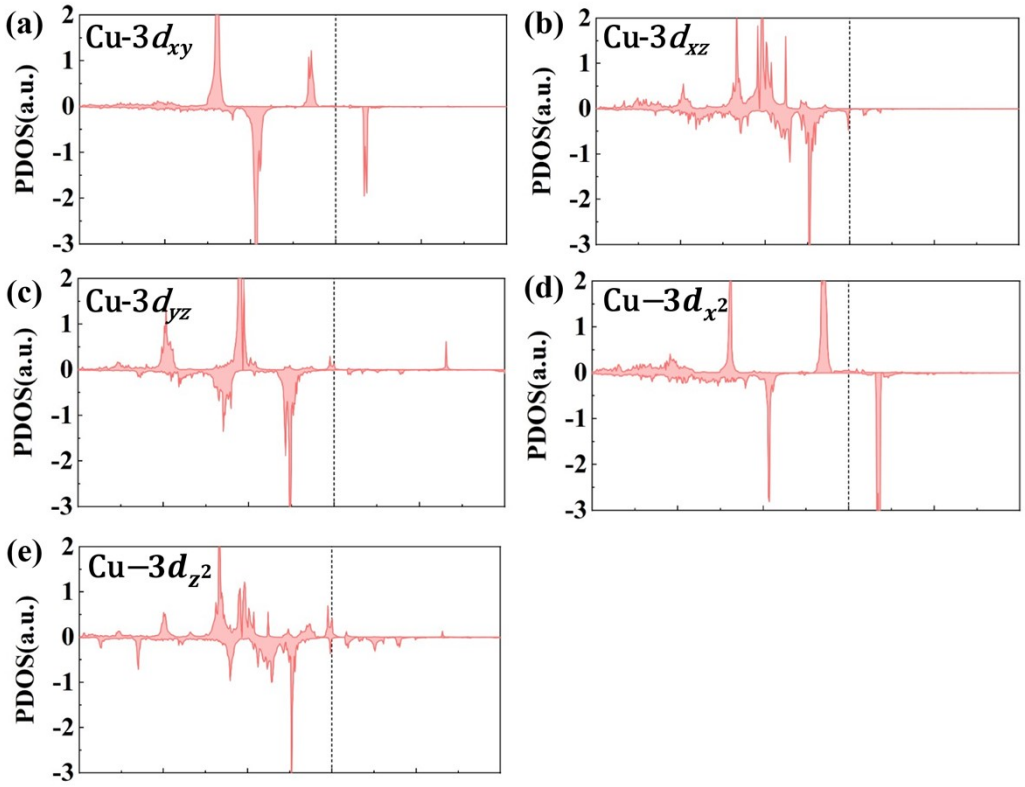

Fig. S18. Cu-N_5-C SAC adsorption of PDOS from the Cu d orbital of the *COOH-NO intermediate.

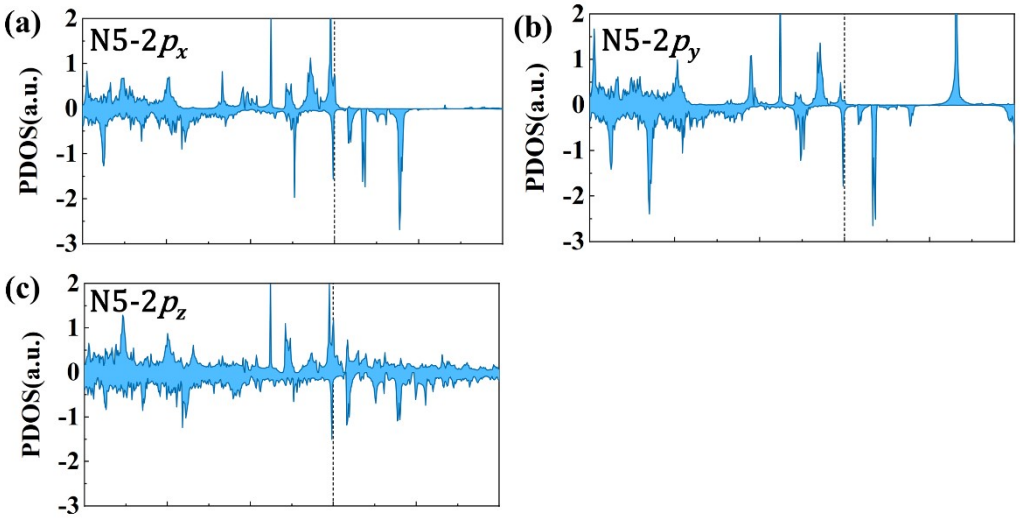

Fig. S19. Cu-N_5-C SAC adsorption of PDOS from the N_5 p orbital of the *COOH-NO intermediate.

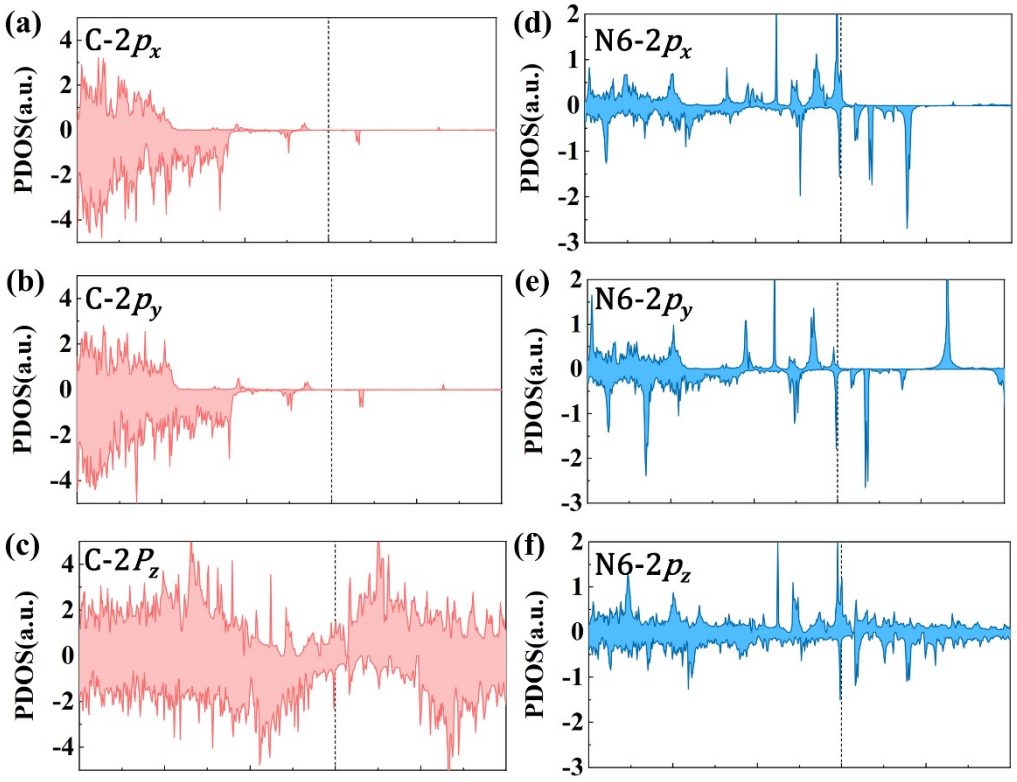

Fig. S20. Cu-N_5-C SAC adsorption of *COOH-NO intermediates C and N_6 p orbitals for PDOS.

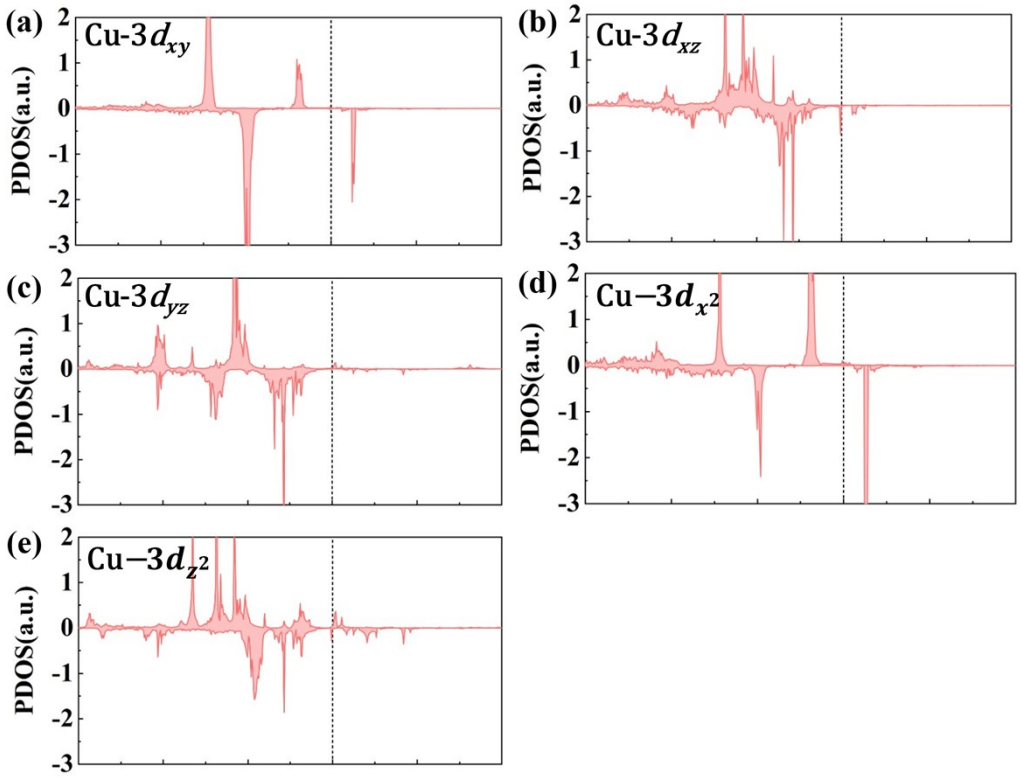

Fig. S21. Cu-N_5-C SAC adsorption of PDOS from the Cu d orbital of the *NH_2-CO-NO intermediate.

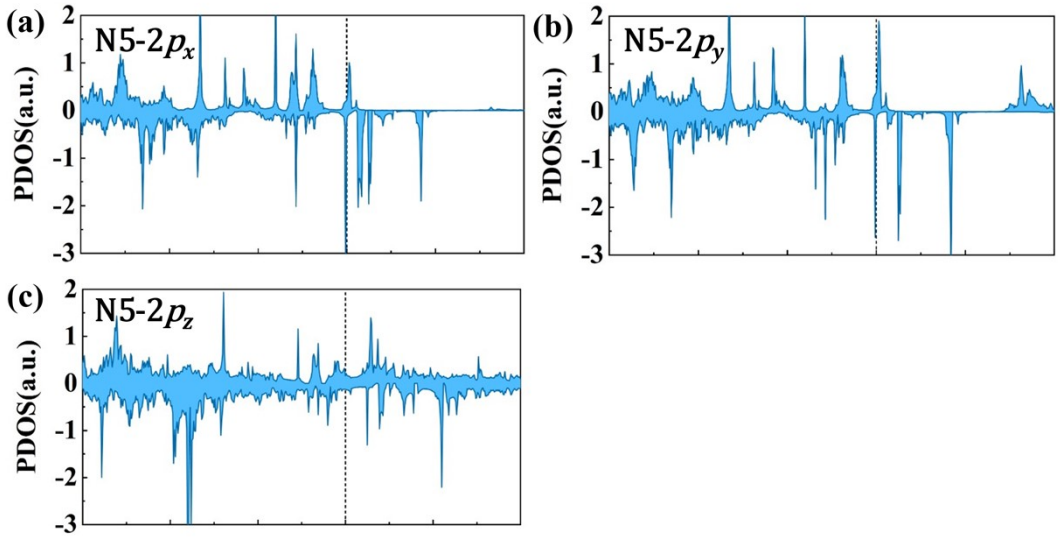

Fig. S22. Cu-N_5-C SAC adsorption of PDOS from the N_5 p orbital of the *NH_2-CO-NO intermediate.

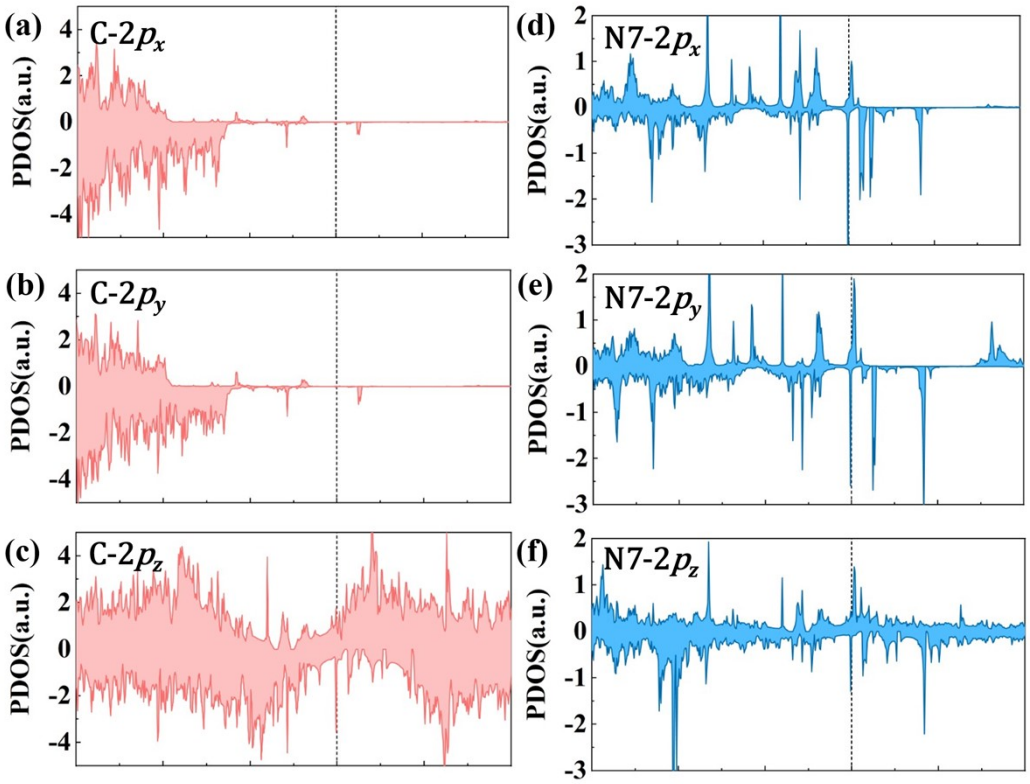

Fig. S23. Cu-N_5-C SAC adsorption of *NH_2-CO-NO intermediates C and N_7 p orbitals for PDOS.

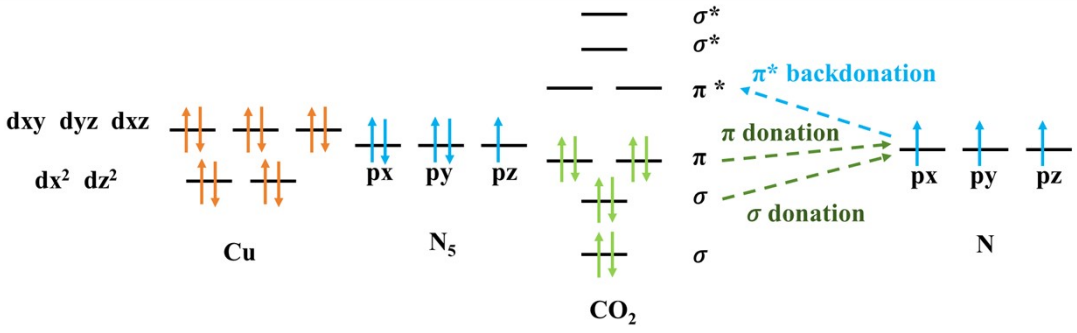

Fig. S24. Schematic of the first step C-N coupling of 3D N_5 in Cu-N_5-C SAC.

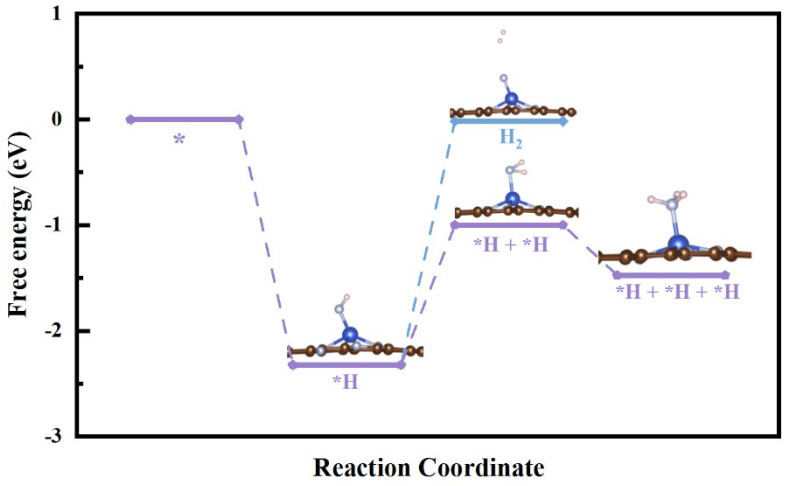

Fig. S25. Step diagram and corresponding structural diagram of axial N being reduced by H.

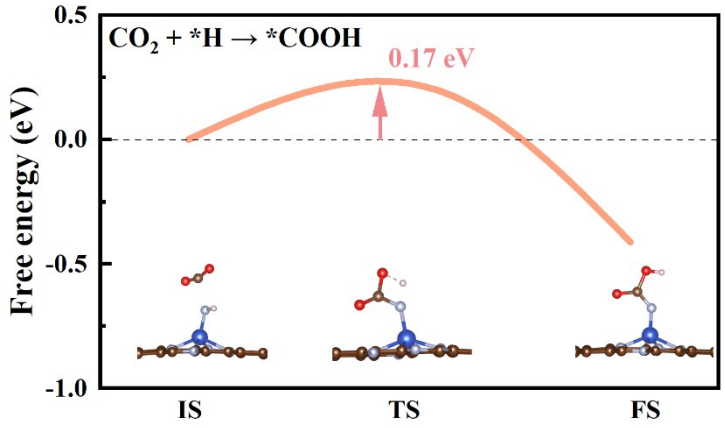

Fig. S26. Energy barrier for the reaction of CO_2 + *H → *COOH.

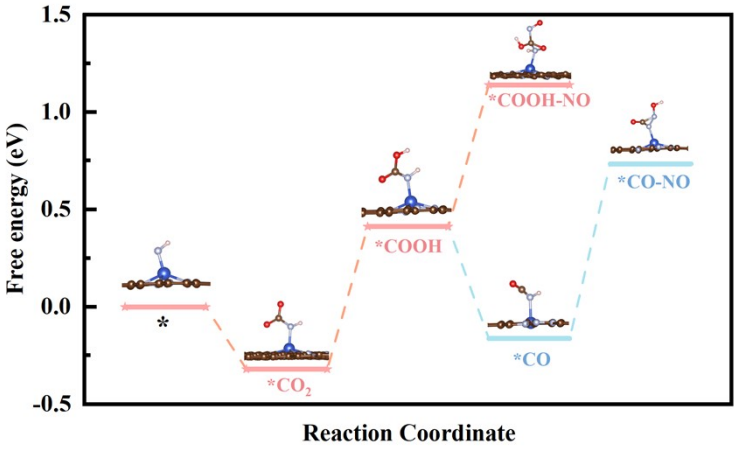

Fig. S27. Free energy changes for electroreduction with NH-axial ligands.

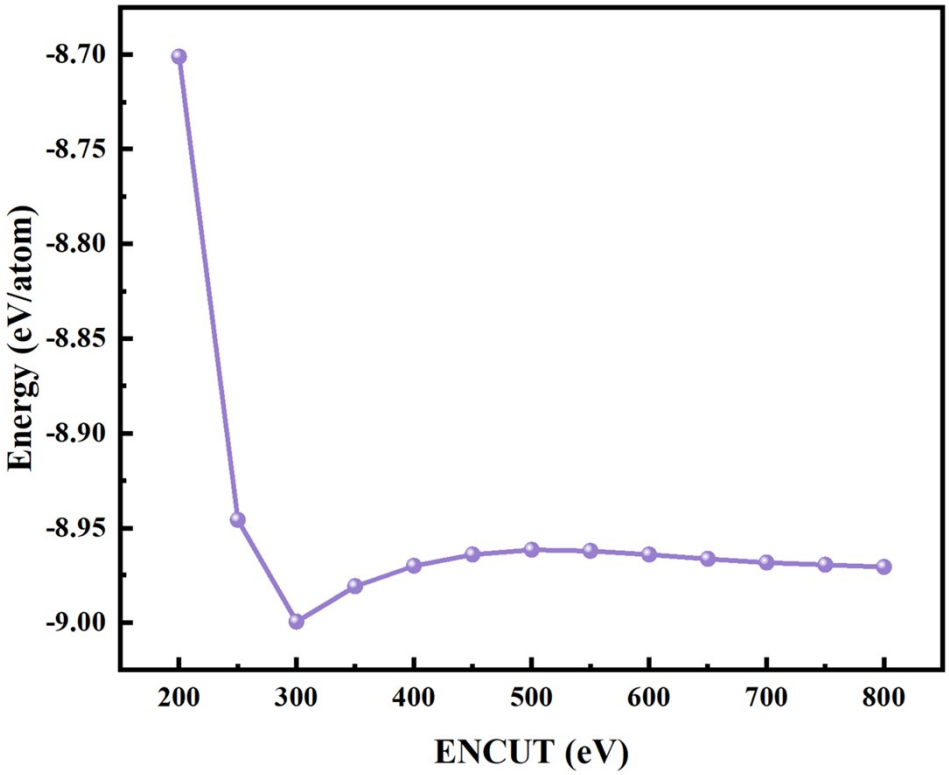

Fig S28. ENCUT testing of Cu-N_5-C SAC.

Tables：

Table S1. The frequency of the transition state for *CO+NH_2→*CO-NH_2.

1f = 100.457281 THz	631.191711 2PiTHz	3350.894197 cm^{-1}	415.457744meV
2f = 97.794862 THz	614.463242 2PiTHz	3262.085476 cm^{-1}	404.446871meV
3f = 60.324397 THz	379.029363 2PiTHz	2012.205282 cm^{-1}	249.481546meV
4f = 45.173439 THz	283.833086 2PiTHz	1506.823721 cm^{-1}	186.822247meV
5f = 23.733581 THz	149.122488 2PiTHz	791.667051 cm^{-1}	98.15416meV
6f = 17.19892 THz	108.064 2PiTHz	573.694214 cm^{-1}	71.128985meV
7f = 16.210354 THz	101.852659 2PiTHz	540.719212 cm^{-1}	67.040608meV
8f = 6.801296 THz	42.7338 2PiTHz	226.866799 cm^{-1}	28.127886meV
9f = 5.233978 THz	32.886051 2PiTHz	174.586702 cm^{-1}	21.645983meV
10f = 2.584393 THz	16.238218 2PiTHz	86.206058 cm^{-1}	10.688184meV
11f = 2.543293 THz	15.979979 2PiTHz	84.835112 cm^{-1}	10.518209meV
12f = 0.962777 THz	6.049304 2PiTHz	32.114773 cm^{-1}	3.981723meV
13f = 0.79413 THz	4.989669 2PiTHz	26.489342 cm^{-1}	3.284258meV
14f = 0.3646 THz	2.290846 2PiTHz	12.161731 cm^{-1}	1.507862meV
15f/i = 0.365308 THz	2.295296 2PiTHz	12.185353 cm^{-1}	1.510791meV

Table S2. The frequency of the transition state for *CO-NH_2+NH_2→*CO-NH_2-NH_2.

1f = 107.307764 THz	674.234568 2PiTHz	3579.401732 cm^{-1}	443.789054 meV
2f = 103.790462 THz	652.134708 2PiTHz	3462.077165 cm^{-1}	429.242669 meV
3f = 100.886734 THz	633.890043 2PiTHz	3365.219207 cm^{-1}	417.233818 meV
4f = 98.204645 THz	617.037981 2PiTHz	3275.754348 cm^{-1}	406.141594 meV
5f = 46.549978 THz	292.482138 2PiTHz	1552.740133 cm^{-1}	192.515154 meV
6f = 44.951524 THz	282.438753 2PiTHz	1499.42143 cm^{-1}	185.90448 meV
7f = 43.346703 THz	272.355366 2PiTHz	1445.890368 cm^{-1}	179.267477 meV
8f = 39.246391 THz	246.592349 2PiTHz	1309.118701 cm^{-1}	162.30996 meV
9f = 30.419942 THz	191.134132 2PiTHz	1014.700041 cm^{-1}	125.806714 meV
10f = 22.356388 THz	140.469326 2PiTHz	745.728818 cm^{-1}	92.458548 meV
11f = 19.963772 THz	125.43608 2PiTHz	665.919759 cm^{-1}	82.56349 meV
12f = 15.157066 THz	95.234655 2PiTHz	505.585301 cm^{-1}	62.68456 meV
13f = 11.292978 THz	70.955876 2PiTHz	376.693214 cm^{-1}	46.703985 meV
14f = 10.797598 THz	67.843309 2PiTHz	360.169099 cm^{-1}	44.655257 meV
15f = 7.533201 THz	47.332496 2PiTHz	251.280526 cm^{-1}	31.154801 meV
16f = 7.111096 THz	44.680334 2PiTHz	237.200631 cm^{-1}	29.409117 meV
17f = 5.628012 THz	35.361843 2PiTHz	187.730279 cm^{-1}	23.275578 meV
18f = 3.138575 THz	19.720249 2PiTHz	104.691595 cm^{-1}	12.980098 meV
19f = 2.699416 THz	16.960928 2PiTHz	90.04281 cm^{-1}	11.163881 meV
20f = 2.166493 THz	13.612477 2PiTHz	72.266426 cm^{-1}	8.959891 meV
21f = 1.360378 THz	8.547507 2PiTHz	45.377325 cm^{-1}	5.626069 meV
22f = 1.091185 THz	6.85612 2PiTHz	36.398025 cm^{-1}	4.512778 meV
23f = 0.506964 THz	3.18535 2PiTHz	16.910507 cm^{-1}	2.096635 meV
24f/i = 0.731313 THz	4.594973 2PiTHz	24.393964 cm^{-1}	3.024465 meV

Table S3. The frequency of the transition state for *COOH+NO→*COOH-NO.

1f = 109.914758 THz	690.614794 2PiTHz	3666.361691 cm^{-1}	454.57071 meV
2f = 50.593035 THz	317.885415 3PiTHz	1687.601998 cm^{-1}	209.235887 meV
3f = 40.312787 THz	253.292711 4PiTHz	1344.689834 cm^{-1}	166.720216 meV
4f = 34.917269 THz	219.391673 5PiTHz	1164.714731 cm^{-1}	144.406157 meV
5f = 31.408319 THz	197.34429 6PiTHz	1047.66876 cm^{-1}	129.894313 meV
6f = 22.930096 THz	144.074041 7PiTHz	764.865668 cm^{-1}	94.831214 meV
7f = 17.136355 THz	107.670894 8PiTHz	571.607275 cm^{-1}	70.870238 meV
8f = 12.651288 THz	79.490385 9PiTHz	422.001531 cm^{-1}	52.321498 meV
9f = 9.894488 THz	62.168901 10PiTHz	330.044593 cm^{-1}	40.920296 meV
10f = 8.83751 THz	55.527714 11PiTHz	294.787605 cm^{-1}	36.548988 meV
11f = 7.577126 THz	47.608487 12PiTHz	252.745717 cm^{-1}	31.336461 meV
12f = 6.557322 THz	41.200868 13PiTHz	218.728713 cm^{-1}	27.118892 meV
13f = 6.052991 THz	38.032063 14PiTHz	201.906039 cm^{-1}	25.033147 meV
14f = 3.045648 THz	19.136371 15PiTHz	101.591881 cm^{-1}	12.595782 meV
15f = 1.412048 THz	8.872161 16PiTHz	47.100861 cm^{-1}	5.83976 meV
16f = 0.831814 THz	5.22644 17PiTHz	27.746318 cm^{-1}	3.440103 meV
17f = 0.168054 THz	1.055912 2PiTHz	5.605667 cm^{-1}	0.695014 meV
18f/i=12.107322 THz	76.072547 2PiTHz	403.856789 cm^{-1}	50.071838 meV

Table S4. The frequency of the transition state for *CO-NH_2+NO→*NH_2-CO-NO.

1f = 104.81997 THz	658.603293 2PiTHz	3496.417832 cm^{-1}	433.500367 meV
2f = 101.616463 THz	638.475065 2PiTHz	3389.56034 cm^{-1}	420.251732 meV
3f = 50.539119 THz	317.546647 2PiTHz	1685.803537 cm^{-1}	209.012906 meV
4f = 47.501486 THz	298.460639 2PiTHz	1584.47902 cm^{-1}	196.450273 meV
5f = 43.452877 THz	273.022481 2PiTHz	1449.431973 cm^{-1}	179.70658 meV
6f = 37.953038 THz	238.465969 2PiTHz	1265.977071 cm^{-1}	156.961082 meV
7f = 31.029209 THz	194.962271 2PiTHz	1035.023006 cm^{-1}	128.32644 meV
8f = 27.081495 THz	170.15805 2PiTHz	903.34143 cm^{-1}	112.000013 meV
9f = 21.299385 THz	133.827982 2PiTHz	710.471004 cm^{-1}	88.087138 meV
10f = 17.521827 THz	110.092884 2PiTHz	584.465228 cm^{-1}	72.46442 meV
11f = 16.073743 THz	100.994306 2PiTHz	536.162356 cm^{-1}	66.47563 meV
12f = 13.720177 THz	86.206411 2PiTHz	457.655826 cm^{-1}	56.742065 meV
13f = 13.142922 THz	82.579416 2PiTHz	438.400698 cm^{-1}	54.354735 meV
14f = 8.72619 THz	54.828269 2PiTHz	291.074369 cm^{-1}	36.088606 meV
15f = 8.128235 THz	51.07121 2PiTHz	271.128751 cm^{-1}	33.615666 meV
16f = 6.634085 THz	41.683183 2PiTHz	221.289243 cm^{-1}	27.436357 meV
17f = 4.89641 THz	30.765051 2PiTHz	163.326656 cm^{-1}	20.249915 meV
18f = 4.727464 THz	29.70353 2PiTHz	157.691212 cm^{-1}	19.55121 meV
19f = 2.897727 THz	18.206956 2PiTHz	96.657768 cm^{-1}	11.98403 meV
20f = 1.942447 THz	12.204753 2PiTHz	64.793049 cm^{-1}	8.033311 meV
21f = 1.346447 THz	8.459976 2PiTHz	44.912639 cm^{-1}	5.568455 meV
22f = 0.90313 THz	5.674533 2PiTHz	30.125173 cm^{-1}	3.735044 meV
23f = 0.363024 THz	2.280948 2PiTHz	12.109183 cm^{-1}	1.501347 meV
24f/i= 12.91528 THz	81.1491012 PiTHz	430.807385 cm^{-1}	53.413284 meV

Table S5. The frequency of the transition state for CO_2+*H→*COOH.

1f = 61.594296 THz	387.008378 2PiTHz	2054.564573 cm^{-1}	254.733427 meV
2f = 45.969007 THz	288.83179 2PiTHz	1533.361028 cm^{-1}	190.112452 meV
3f = 33.637454 THz	211.350357 2PiTHz	1122.024691 cm^{-1}	139.113269 meV
4f = 23.331145 THz	146.593909 2PiTHz	778.243234 cm^{-1}	96.48982 meV
5f = 22.639443 THz	142.247818 2PiTHz	755.170547 cm^{-1}	93.629173 meV
6f = 19.772175 THz	124.232238 2PiTHz	659.52876 cm^{-1}	81.771108 meV
7f = 13.989975 THz	87.901604 2PiTHz	466.655328 cm^{-1}	57.857861 meV
8f = 11.107424 THz	69.790002 2PiTHz	370.503777 cm^{-1}	45.936593 meV
9f = 3.065236 THz	19.259445 2PiTHz	102.245265 cm^{-1}	12.676791 meV
10f = 1.438745 THz	9.039899 2PiTHz	47.991356 cm^{-1}	5.950167 meV
11f = 0.706849 THz	4.441266 2PiTHz	23.577959 cm^{-1}	2.923293 meV
12f/i = 50.6294 THz	318.113903 2PiTHz	1688.815006 cm^{-1}	209.38628 meV

References:

[1] G. Kresse, J. Furthmüller, Efficiency of ab-initio total energy calculations for metals and semiconductors using a plane-wave basis set. Comput. Mater. Sci. 1996, 6:5-50.

[2] V. Wang, N. Xu, J. Liu, G. Tang, W. Geng, VASPKIT: A user-friendly interface facilitating high-throughput computing and analysis using VASP code. Comput. Phys. Commun. 2021, 267:108033.

[3] K. Momma, Lzumi. F, VESTA 3 for three-dimensional visualization of crystal, volumetric and morphology data. J. Appl. Crystal. 2011, 44:1272-1276.

[4] S. Grimme, J. Antony, S. Ehrlich, A consistent and accurate ab initio parametrization of density functional dispersion correction (DFT-D) for the 94 elements H-Pu. J. Chem. Phys, 2010, 132.

[5] J. Monkhorst, D. Pack, Special points for Brillouin-zone integrations. Phys Rev B, 1976, 13: 5188.

[6] M. Egon, G. Robert, Surface and colloid science. Springer Science & Business Media, 2012, 12.

[7] V. Wang, N. Xu, J. Liu, G. Tang, W. Geng, VASPKIT: A user-friendly interface facilitating high-throughput computing and analysis using VASP code. Comput. Phys. Commun., 2021, 267: 108033.

[8] S. Maintz, L. Deringer, L. Tchougréeff, LOBSTER: A tool to extract chemical bonding from plane-wave based DFT. J. Comput. Chem. 2016, 37: 1030-1035.

[9] X. Liu, Y. Jiao, Y. Zheng, M. Jaroniec, Z. Qiao, Mechanism of C-N bonds formation in electrocatalytic urea production revealed by ab initio molecular dynamics simulation. Nat Commun. 2022, 13, 5471.